Bioactive Materials 35 (2024) 67–81

Contents lists available at ScienceDirect

Bioactive Materials

journal homepage: www.keaipublishing.com/en/journals/bioactive-materials

Nano oxygen chamber by cascade reaction for hypoxia mitigation and reactive oxygen species scavenging in wound healing

Xiaoxue Han [a,b,c], Leah Ju [a,b], Chai Saengow [f], Wen Ren [a,b,c], Randy Ewoldt [f], Timothy Fan [c,e], Joseph Irudayaraj [a,b,c,d,*]

[a] Department of Bioengineering, 1102 Everitt Lab, 1406 W. Green St., University of Illinois at Urbana-Champaign, Urbana, IL, 61801, USA
[b] Biomedical Research Center, Mills Breast Cancer Institute, Carle Foundation Hospital, Urbana, IL, 61801, USA
[c] Cancer Center at Illinois, Beckman Institute, Urbana, IL, 61801, USA
[d] Carle Illinois College of Medicine, University of Illinois at Urbana-Champaign, Urbana, IL, 61801, USA
[e] Department of Veterinary Clinical Medicine, College of Veterinary Medicine, University of Illinois at Urbana-Champaign, Urbana, IL, 61801, USA
[f] Department of Mechanical Science and Engineering, University of Illinois at Urbana-Champaign, Urbana, IL, USA

ARTICLE INFO

Keywords:
Hypoxia
ROS scavenging
Anti-inflammation
Oxygen nanobubble
Scarless wound healing

ABSTRACT

Hypoxia, excessive reactive oxygen species (ROS), and impaired angiogenesis are prominent obstacles to wound healing following trauma and surgical procedures, often leading to the development of keloids and hypertrophic scars. To address these challenges, a novel approach has been proposed, involving the development of a cascade enzymatic reaction-based nanocarriers-laden wound dressing. This advanced technology incorporates superoxide dismutase modified oxygen nanobubbles and catalase modified oxygen nanobubbles within an alginate hydrogel matrix. The oxygen nano chamber functions through a cascade reaction between superoxide dismutase and catalase, wherein excessive superoxide in the wound environment is enzymatically decomposed into hydrogen peroxide, and this hydrogen peroxide is subsequently converted into oxygen by catalase. This enzymatic cascade effectively controls wound inflammation and hypoxia, mitigating the risk of keloid formation. Concurrently, the oxygen nanobubbles release oxygen continuously, thus providing a sustained supply of oxygen to the wound site. The oxygen release from this dynamic system stimulates fibroblast proliferation, fosters the formation of new blood vessels, and contributes to the overall wound healing process. In the rat full-thickness wound model, the cascade reaction-based nano oxygen chamber displayed a notable capacity to expedite wound healing without scarring. Furthermore, in the pilot study of porcine full-thickness wound healing, a notable acceleration of tissue repair was observed in the conceived cascade reaction-based gel treated group within the 3 days post-surgery, which represents the proliferation stage of healing process. These achievements hold significant importance in ensuring the complete functional recovery of tissues, thereby highlighting its potential as a promising approach for enhancing wound healing outcomes.

1. Introduction

The rapid and successful healing of traumatic and surgical wounds is a formidable task that carries considerable implications for a substantial global demographic, thereby exerting significant pressures on healthcare infrastructures and patients alike [1]. Not only does this process intricately influence individuals' psychological and physiological well-being, but it also imparts substantial financial ramifications due to the need for prolonged wound management strategies [2]. Consequently, this culminates in a notable societal burden. Further exacerbating this intricate issue is the frequent emergence of keloids and hypertrophic scars, which complicates wound recovery scenarios [3]. The formation of keloids not only disrupts the functional integrity of the regenerated tissue but also profoundly undermines the overall quality of life experienced by affected individuals [4,5].

Amid the multitude of factors contributing to inadequate healing and the formation of keloids, excessive inflammation emerges as a pivotal causative element [6]. While low levels of reactive oxygen species (ROS) are essential for defending against external pathogens in normal physiological environment, an elevated ROS level in poorly healed wounds

Peer review under responsibility of KeAi Communications Co., Ltd.
* Corresponding author. Department of Bioengineering, 1102 Everitt Lab, 1406 W. Green St., University of Illinois at Urbana-Champaign, Urbana, IL, 61801, USA.
E-mail address: jirudaya@illinois.edu (J. Irudayaraj).

https://doi.org/10.1016/j.bioactmat.2024.01.010
Received 22 October 2023; Received in revised form 26 December 2023; Accepted 11 January 2024

leads to persistent and irreversible damage in the affected area [7]. This, in turn, initiates oxidative stress and exacerbates the inflammatory response, thereby sustaining macrophages in the M1 phenotype. Notably, a panel of molecules such as IL-6, IL-8, and IL-18, have been identified as significantly upregulated in keloid tissue, eliciting pronounced pro-inflammatory effects following tissue damage [8]. This pronounced inflammatory milieu is not confined to keloid tissue alone; even in the peripheral blood of keloid-afflicted individuals, IL-8 levels have been observed to surge up to seven-fold higher than those in healthy individuals [9]. To surmount this formidable challenge, various anti-inflammatory strategies have been devised and implemented within wound dressings [10]. An emergent approach lies in the realm of nanoenzymes, synthetic nanomaterials endowed with enzyme-mimicking attributes, known for their potent catalytic efficiency and robust stability [11]. However, the translation of nanoenzymes into clinical applications has been hindered by several constraints. While diverse methodologies have emerged for the meticulous fabrication of nanozymes with well-defined structures, a paucity of comprehensive insights into their underlying catalytic mechanisms persists [12]. Furthermore, the enhancement of nanozyme selectivity and activity remains a paramount goal, and the uncertainty of biocompatibility, safety and therapeutic efficacy poses a formidable challenge that necessitates further inquiry [13].

Hypoxia constitutes an additional pivotal contributor to the impairment of wound healing and the emergence of keloids [14]. To increase wound oxygen level, diverse approaches have been explored, including hyperbaric oxygen therapy (HBOT), topical oxygen therapy (TOT) devices and dressings in clinical wound management such as OxyBand (OxyBand Technologies) and O_2Boot (GWR Medical Inc.) [15,16]. Despite these advancements, the efficacy of HBOT and TOT was limited by the restricted penetration of external gases into tissues, the potential side effects, and the lack of precision in controlling oxygen delivery further constrains their potential [17,18]. To address these challenges, novel nanotechnologies for enhancing wound oxygenation have come to the forefront, including (1) oxygen generation through enzymatic reactions based on catalase, MnO_2, or nanoenzymes [19], (2) the utilization of oxygen-carrying materials, including perfluorocarbons, hemoglobin, and oxygen nanobubbles (ONBs) [20]. ONBs, characterized by encapsulating oxygen within shells predominantly crafted from materials such as polymers or lipids, offer a promising avenue for mitigating hypoxia and facilitating wound oxygenation [21,22]. Notably, ONBs exhibit a distinct advantage over dissolved oxygen, since they possess the capacity to retain oxygen over extended periods when situated within an appropriate buffer [23].

With the aim of addressing the dual challenges posed by excessive inflammation and hypoxia within wounds, we have introduced a novel approach involving the development of a cascade enzymatic reaction-based oxygen-delivering nano chamber, embedded within an alginate hydrogel (see Scheme 1). The nano chamber, which comprises of superoxide scavenging (SOS) oxygen nanobubble and oxygen-generating catalyst (OGC) nanobubble, is constructed by encapsulating nanoscale oxygen bubbles within a glycosylated protein conjugate featuring

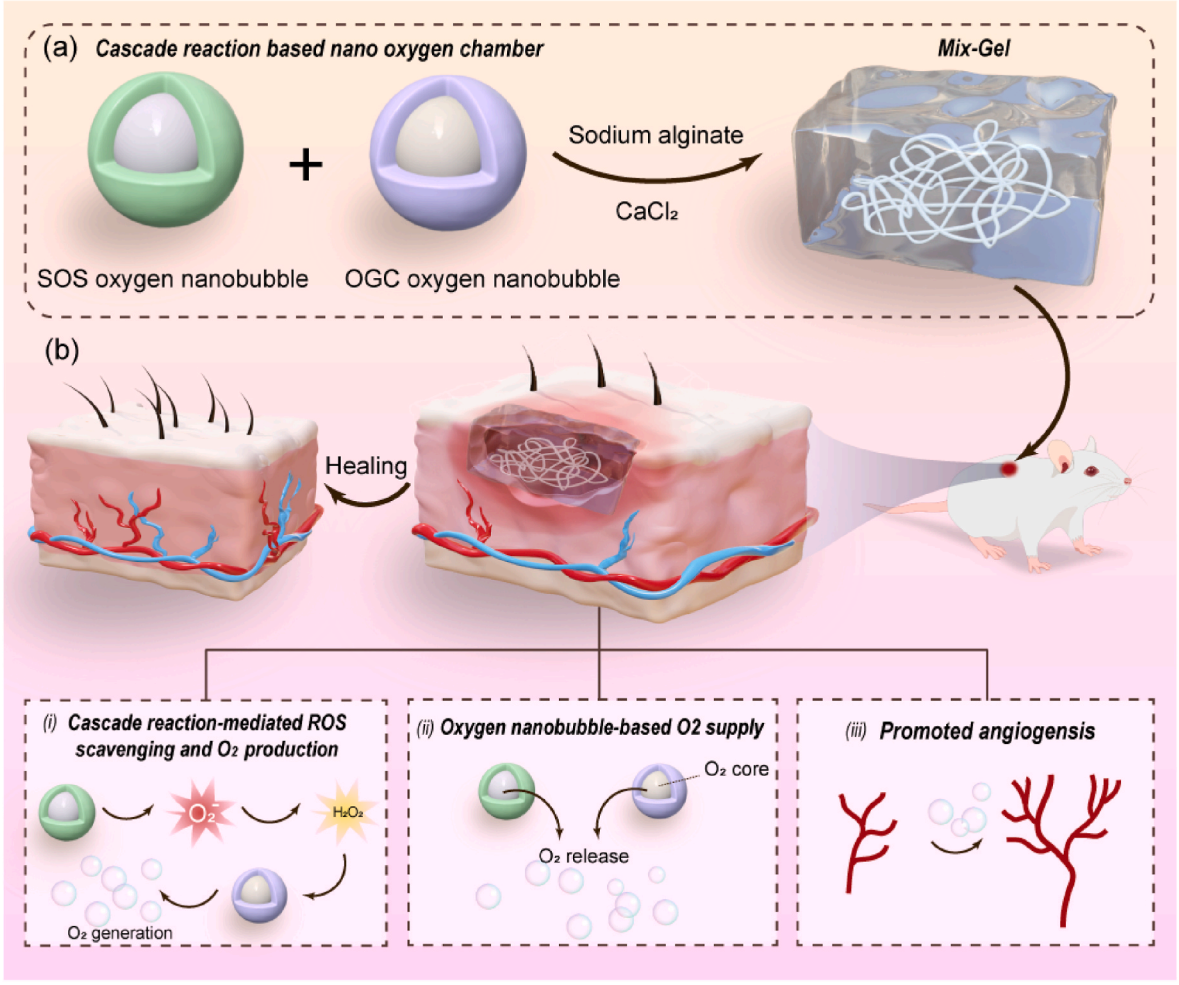

Scheme 1. Schematic illustration of (a) the structure of Mix-Gel and (b) the mechanisms of enhanced healing through (i) cascade enzymatic reaction-mediated ROS scavenging and oxygen production; (ii) oxygen release from the core of cascade reaction-based nano chamber; (iii) enhanced angiogenesis.

dextran-conjugated superoxide dismutase (SOD) and catalase (CAT). The glycosylated proteins have been proven to augment protein properties, fostering improved thermal stability and self-assembling properties [24,25]. Furthermore, the glycosylated protein conjugate serves as the host for the bulk nanoscale oxygen bubbles generated through ultrasonic cavitation, leading to the formation of both SOS and OGC. Functionally, the cascade enzymatic process driven by SOS induces the dismutation of superoxide anions into hydrogen peroxide, which is then effectively converted into oxygen and water through the catalase in OGC. This sequential enzymatic reaction not only addresses reactive oxygen species (ROS) accumulation but also facilitates oxygen generation, thus alleviating hypoxia within the poor healed wound. Furthermore, catalase exhibits highest activity at 35 °C, consistent with the physiological temperatures [26]. Its stability diminishes beyond a pH of 10, and maximal decomposition of H_2O_2 remains consistent until below a pH of 5, with an optimal pH at 7.0 [27]. Considering that wound beds tend to maintain a pH range of 7.2–7.7 [28], the encapsulated catalase-based nanobubble in our wound dressing provides optimal functionality. In parallel, the encapsulated oxygen nanobubbles persistently supply and release oxygen. By combining these two oxygen delivery modalities—the cascade enzymatic oxygen generation and the oxygen nanobubble-mediated oxygen release—the nano chamber exhibits enhanced efficiency in replenishing oxygen to the wound site. This multifaceted nano chamber is incorporated into an alginate hydrogel matrix (Mix-Gel), which is then applied to the wounded area. Notably, our method has been proven efficacious in the acceleration of wound closure in both rat and porcine full-thickness wound models. Moreover, in rat models, the approach showcases a remarkable achievement in obtaining scarless wound that healed within 14 days of treatment.

2. Results

2.1. Synthesis and characterization of SOS, OGC, and hydrogels

The fabrication process of SOS and OGC oxygen nanobubble follows a previously reported methodology with slight modifications [29]. Briefly, the synthesis initiated with the conjugation of SOD and CAT to dextran sulfate induced by 24 h of mixing and subsequent ultrasonication. Concurrently, oxygen was introduced into the system and nanobubbles were generated during ultrasonication. The conjugated superoxide dismutase was measured using bicinchoninic acid (BCA) protein assay (Fig. S2). Dynamic light scattering (DLS) analysis indicated that SOS exhibited an average hydrodynamic diameter of 59.40 nm and a mean zeta potential of −38.94 mV (Fig. 1a and c). The rounded morphology was observed using scanning electron microscopy (SEM) (Fig. S3). Transmission electron microscopy (TEM) imaging further validated the core-shell configuration of SOS, featuring a protein-polymer shell negatively stained and an oxygen nanobubble

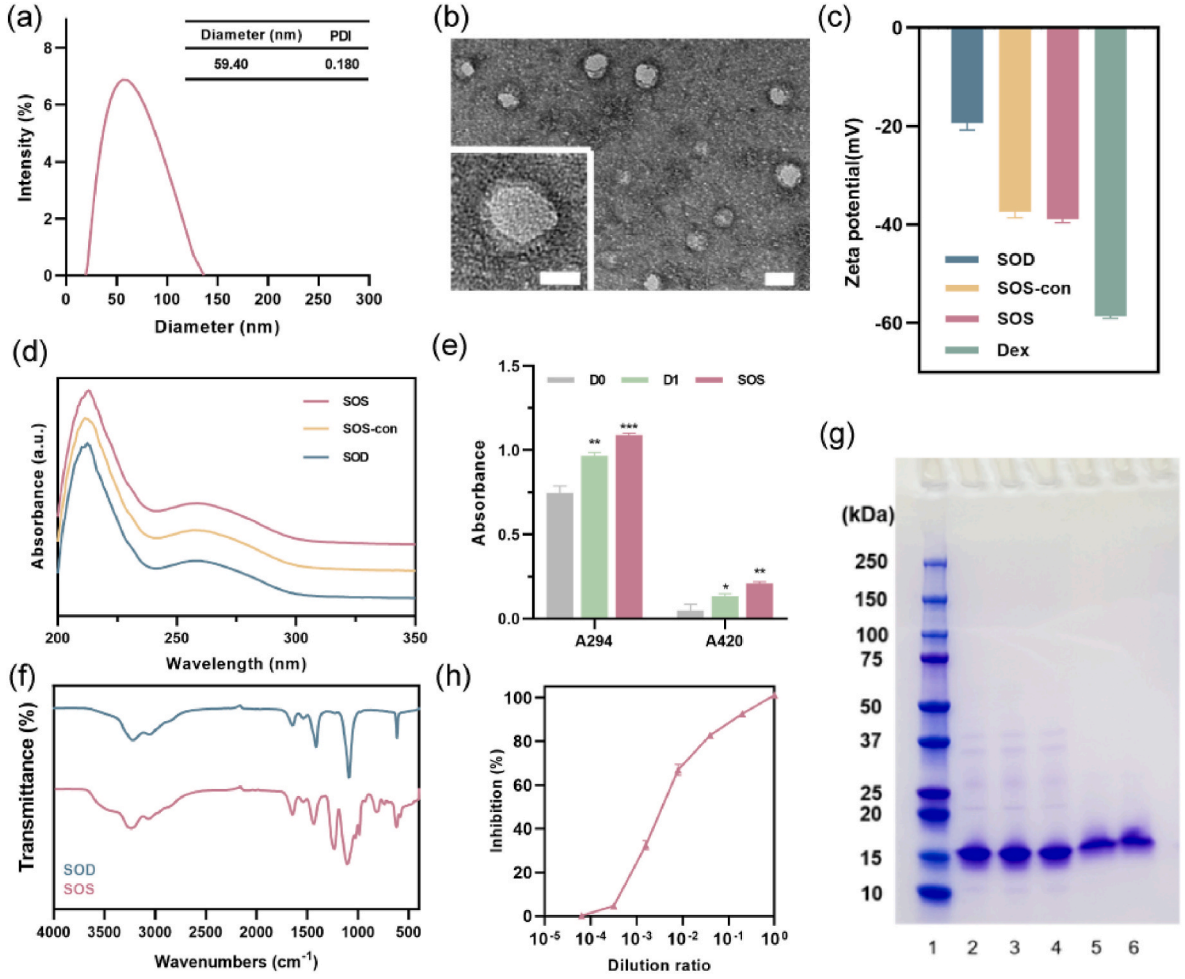

Fig. 1. Characterization of SOS. (a) Diameter distribution and polydispersity index (PDI) of SOS. (b) TEM image of SOS. Scale bar = 50 nm and 20 nm (magnified image). (c) Zeta potential of SOS (n = 3, mean ± SD). (d) UV–vis absorbance of SOS, SOS-con, and SOD. (e) A294 and A420 of: mixture of dextran sulfate and SOD (D0), mixture of dextran sulfate and SOD following 24 h of mixing, and SOS (n = 3, mean ± SD). (f) Infrared spectra of SOD and SOS. (g) Gel electrophoresis of different samples. Lanes: 1: Protein ladder; 2: Natural SOD; 3: Mixture of dextran sulfate and SOD; 4: Ultrasonicated SOD; 5: SOS-con; 6: SOS. (h) Inhibition of WST-1 reduction rate (n = 3, mean ± SD).

core (Fig. 1b). The distinct absorption peaks of SOD at approximately 210 nm and 258 nm were evident in both SOS and SOS-con as well, confirming the presence of SOD in the SOS structure. Likewise, DLS analysis indicated that the OGC oxygen nanobubble exhibited a diameter of 97.73 nm and a zeta potential of −25 mV (Figs. S1a and S1b). TEM imaging also confirmed that OGC possessed a similar core-shell structure compared to SOS (Fig. S1c). UV–vis absorption demonstrated similar characteristic peaks of SOD and CAT in the formulations, which verified the presence of enzyme in the SOS and OGC (Fig. 1d and Fig. S1d). Concentration distribution of SOS was measured using nanoparticle tracking analysis (NTA) (Fig. S4) and 4 °C stability of OGC and SOS was monitored for a period if six weeks. Results revealed high size stability of both OGC and SOS, favorable for practical applications (Fig. S5).

To further verify the formation of SOS and OGC, the successful conjugation between dextran sulfate and enzymes was assessed. UV–vis absorbance at 294 nm and 420 nm (Fig. 1e) was measured to evaluate the intensity of browning, indicative of early and late Maillard reaction products (MRP), respectively [30]. The results revealed a notable rise in absorbance at both 294 nm and 420 nm following 24 h of mixing, in comparison to non-ultrasonicated SOD at day zero (D0). Following ultrasonication, the absorbance was further elevated, thereby affirming the formation of MRP products. Fig. S1e also demonstrated consistent findings, with both A294 and A420 showing higher values in OGC compared to CAT. Fig. 1f and Fig. S1f displays the FT-IR spectra of both native enzyme and enzymatic oxygen nanobubble. The absorption bands observed at 1645 cm^{-1} and 1540 cm^{-1} were attributed to the distinct amide I and amide II bands inherent to proteins [31]. These spectral features represent well-characterized structural features of proteins. The presence of a wide band around 3411 cm^{-1} indicated O–H stretching, while a distinct sharp band observed at approximately 1024 cm^{-1} was attributed to C–O stretching [31,32]. These spectral characteristics suggest that the introduction of dextran sulfate through covalent binding brought about the incorporation of sugar molecules, thus providing additional confirmation of the formation of glycosylated protein conjugates. Sodium dodecyl sulfate–polyacrylamide gel electrophoresis (SDS-PAGE) analysis was performed to further confirm the conjugation. The sample of native SOD displayed a band at approximately 16 kDa, consistent with the monomeric form of SOD (with a molecular weight of 16.8 kDa). Comparable protein bands were detected in the remaining samples, including the mixture, sonicated SOD, SOS-con, and SOS samples, indicating the presence of SOD within these formulations. Notably, the protein bands of SOS-con and SOS exhibited a slight shift towards higher molecular weights compared to native SOD, which can be attributed to the increased molecular mass resulting from the successful conjugation between the protein and polysaccharides induced by ultrasonication, thereby confirming the effective formation of SOS (Fig. 1g). Subsequently, the SOD catalytic activity of both SOS and SOS-con was assessed using the WST-1 (2-(4-iodophenyl)-3-(4-nitrophenyl)-5-(2,4-disulfo-phenyl)-2H-tetrazolium, monosodium salt) assay [33,34]. The results demonstrated that both SOS and SOS-con effectively inhibited the reduction of WST-1 induced by superoxide anion (Fig. 1h, Fig. S6). Remarkably, even when diluted 25 times, the inhibition rate remained consistently above 80 %. Overall, these findings collectively confirm the successful formation of SOS, with the retained SOD activity and the ability to effectively scavenge superoxide anions.

Considering clinical safety and translation, sodium alginate (SA), FDA-approved material, was employed as the skeleton of Mix-Gel [35]. The imperative attributes of clinical hydrogel dressings include excellent fluidity and gelling proficiency [36]. Hence, we investigated the impact of varying concentrations of alginate on the gel properties. The data from the time sweep analysis revealed that different concentrations of alginate did not have a substantial influence on the gelation time (Fig. S7). Subsequent SEM imaging analysis, digital photos, and rheological properties indicated that higher alginate concentrations resulted in a denser micropore structure, but concurrently increased stiffness, which is not conducive for wound application (Figs. S8, S9, S10). Considering these findings collectively, we selected a final concentration of 1 wt% for our subsequent experiments. To ascertain the optimal conditions for the cascade reaction, different ratios of SOD to CAT was utilized to measure the concentration of hydrogen peroxide (H_2O_2), the intermediate product of the cascade reaction. Notably, we observed a diminishing effect of the cascade reaction when the SOD:CAT ratio was lowered from 1:2 to 1:0.5, suggesting a lower turnover number of CAT compared to SOD (Fig. S11). Further increasing the ratio to 1:4 did not significantly enhance the cascade reaction, possibly due to the high concentrations within the confined in vitro experimental setup. Consequently, the concentration ratio of SOD:CAT at 1:2 was deemed optimal and used in subsequent experiments. The image of Mix-Gel applied to the upper arm is depicted in Fig. S12. The transparency of the gel facilitates continuous monitoring of the wound condition. Nanobubble release profile within 48 h was investigated in PBS (pH = 7.4) at 37 °C (Fig. S13). Scanning electron microscopy (SEM) imaging revealed the microstructure of hydrogels. Blank-Gel, OGC-Gel, SOS-Gel, and Mix-Gel all displayed a pore-structure with similar pore size (Fig. 2a). The laden nanoparticles can be visualized in the structure. To preempt premature oxygen leakage from the cascade reaction nano chamber, it was imperative for the hydrogel matrix to exhibit swift gelation characteristics. Consequently, rheological properties were investigated based on the strain-amplitude sweep because the frequency dependency of alginate gels with a $CaCl_2$ crosslinker is mild [37]. As the strain-amplitude was increased, the Mix-Gel and other hydrogels exhibited a similar pattern where the storage modulus (G′) values consistently surpassed their corresponding loss modulus (G″) values, suggesting the prevailing elastic-dominated characteristics of these hydrogels (Fig. 2b and d). The incorporation of nanoparticles did not result in significant alterations in the overall mechanical properties. The results of the time sweep analysis demonstrated that both the Mix-Gel and other hydrogels underwent gelation within a mere 100 s (Fig. 2c and e). This rapid gelation timeframe ensures the prevention of oxygen leakage prior to application onto wounds.

2.2. Oxygen production and ROS scavenging

In theory, the cascade enzymatic reaction-based oxygen nano chamber has the potential to efficiently convert reactive oxygen species (ROS) including superoxide anion and H_2O_2 into oxygen. To validate this, the process of oxygen production was visualized and subsequently monitored using a dissolved oxygen meter (Fig. 3a and b). Following incubation, with a mixture of H_2O_2 and superoxide anion, comparison with Blank-Gel revealed that both Mix-Gel and OGC-Gel prominently generated a substantial quantity of gas bubbles, causing them to float. SOS-Gel also yielded a minor number of bubbles, which can be attributed to the limited amount of oxygen produced through the decomposition of superoxide anion. Oxygen generation was evaluated over a 48-h period to align with the dressing renewal schedule in the in vivo rat full-thickness wound model. Our findings indicate that, among the tested hydrogels, Mix-Gels exhibited the highest capacity for oxygen production, reaching up to 8.96 mg/L. This notable oxygen generation can be attributed to the dual mechanisms employed, including the cascade enzymatic reaction-based oxygen production mode and the release of encapsulated oxygen nanobubbles. The evaluation of intracellular oxygen supply was conducted on HDFa (Human Dermal Fibroblasts, adult) cells using a cellular hypoxia indicator, [Ru(dpp)3]Cl2 (RDPP) (Fig. 3c). The HDFa cells treated with Mix-Gel exhibited the lowest RDPP fluorescence, resembling the levels observed in cells incubated under normoxia. This observation indicates the attenuation of hypoxia, thus confirming the efficacy of the Mix-Gel in providing an effective oxygen supply mechanism.

Mix-Gel is expected to possess the capability to decompose superoxide anions, with the resultant H_2O_2 subsequently being converted into

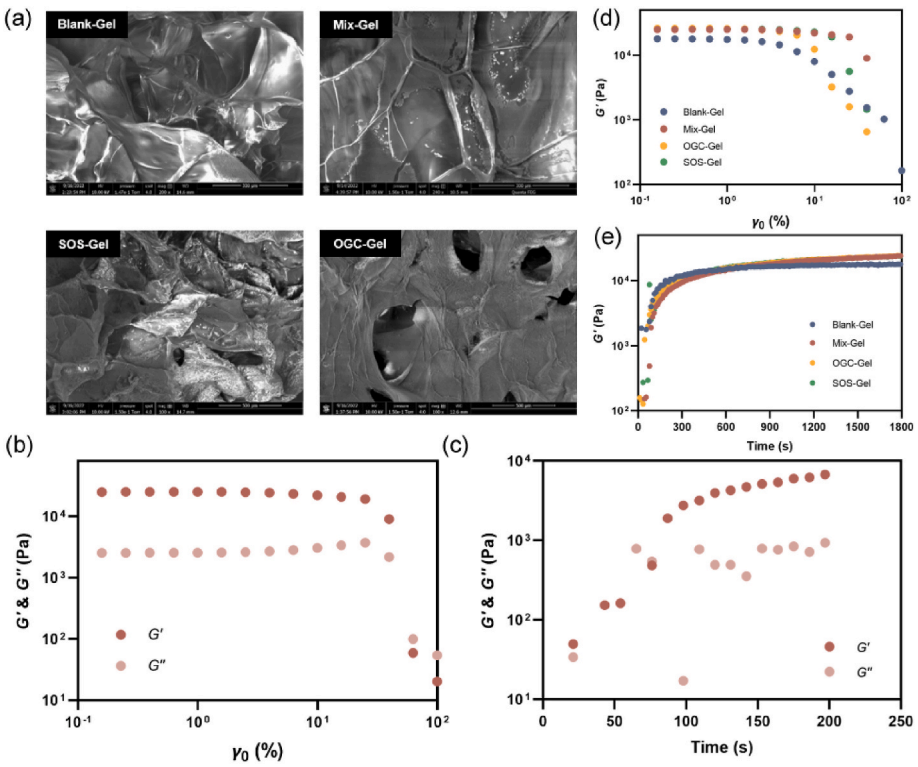

Fig. 2. Characteristics of hydrogels. (a) SEM images of Blank-Gel, Mix-Gel, SOS-Gel, and OGC-Gel. (b) Rheological behaviors (storage modulus and loss modulus) of Mix-Gel. (c) Time sweep analysis of Mix-Gel. Comparative (d) rheological behavior and (e) time sweep of Mix-Gel and other hydrogels.

O_2 through the action of the nano oxygen chamber. The elimination of superoxide anions was evidenced through a WST-1 reduction assay. Comparable to the SOD group, superoxide anions were nearly entirely depleted within 25 min of the reaction in the Mix-Gel (Fig. 3d). Over the 25-min period, absorbance at 450 nm was measured every 5 min (Fig. 3e). The progressively decreasing absorbance indicated the consumption of superoxide anions by the Mix-Gel. Intracellular ROS levels and SOD scavenging were assessed in HDFa cells. ROS indicator, 2′, 7′-dichlorodihydrofluorescein diacetate (H_2DCFDA) staining results revealed that Mix-Gel exhibited the lowest ROS levels among all treatment groups, while OGC-Gel and SOS-Gel also led to a reduction in ROS levels to varying degrees (Fig. 3h). Fluorescent imaging and quantitation further confirmed the comparable efficiency of ROS and SOD scavenging by Mix-Gel, aligning consistently with the previous findings (Fig. 3f and g).

2.3. Evaluation of biocompatibility and enhanced cell proliferation

Biocompatibility studies are crucial for successful clinical translation. In order to assess biocompatibility, cell toxicity assays were conducted on HDFa and HEKa (Human Epidermal Keratinocytes, adult) cells (Fig. 4b, Fig. S14). The results revealed that cell viability remained above 80 % for all hydrogel treatments on both HDFa and HEKa cells, indicating a high level of biocompatibility. Subsequently, a hemolysis assay was conducted to assess blood compatibility (Fig. 4c). Notably, all hydrogel groups exhibited negligible hemolysis, with a hemolytic ratio lower than 2 % [38,39]. These results collectively underscore the remarkable biocompatibility of the hydrogels.

The evaluation of cell proliferation was conducted on HDFa cells, subjected to a 24-h exposure to hypoxic conditions with treatments of different hydrogels. The results showed that Mix-Gel treated cells displayed a discernible increase in cell proliferation among all treatments (Fig. 4d). The live/dead staining assay exhibited a greater proportion of viable cells of the Mix-Gel treatment group, thereby reinforcing the previous observation (Fig. 4a). To further validate the enhanced cell proliferation effect, a BrdU incorporation assay was performed to visualize the newly proliferated cells (Fig. 4e). Remarkably, the Mix-Gel treated group showcased a considerably elevated positive signal of BrdU, indicative of the incorporation of newly synthesized DNA, thereby providing robust evidence of the enhanced proliferation effect induced by Mix-Gel.

2.4. In vitro enhanced wound healing: migration and angiogenesis assessment

In vitro wound healing efficacy was assessed by evaluating cell migration. In the scratch assay, after generating the wound scar, cells were exposed to different treatments under hypoxic conditions and wound closure was visually monitored at 0, 12, and 24 h, respectively. Notably, the Mix-Gel treatment group exhibited the most rapid rate of wound closure compared to all other treatments, highlighting an enhanced cell migration response (Fig. 5a and b). Correspondingly, in the transwell migration assay, the Mix-Gel treatment group also demonstrated a higher count of migrated cells after 24 h of co-incubation, validating the accelerated in vitro wound healing effect of Mix-Gel (Fig. 5c and d).

To assess the in vitro angiogenesis potential, Human Umbilical Vein Endothelial Cells (HUVECs) were employed, as compromised angiogenesis has been associated with delayed wound healing (Fig. 5e). In the tube formation assay, following 6 h of treatments under hypoxic conditions, the group treated with Mix-Gel showed a notable increase in the overall length of branches and the number of branches (Fig. 5f and g). This result demonstrated the capacity of Mix-Gel to promote angiogenesis, suggesting its potential to enhance wound healing.

2.5. In vivo wound healing efficacy on rat full-thickness wound model

A Sprague-Dawley rat model with excisional full-thickness wounds

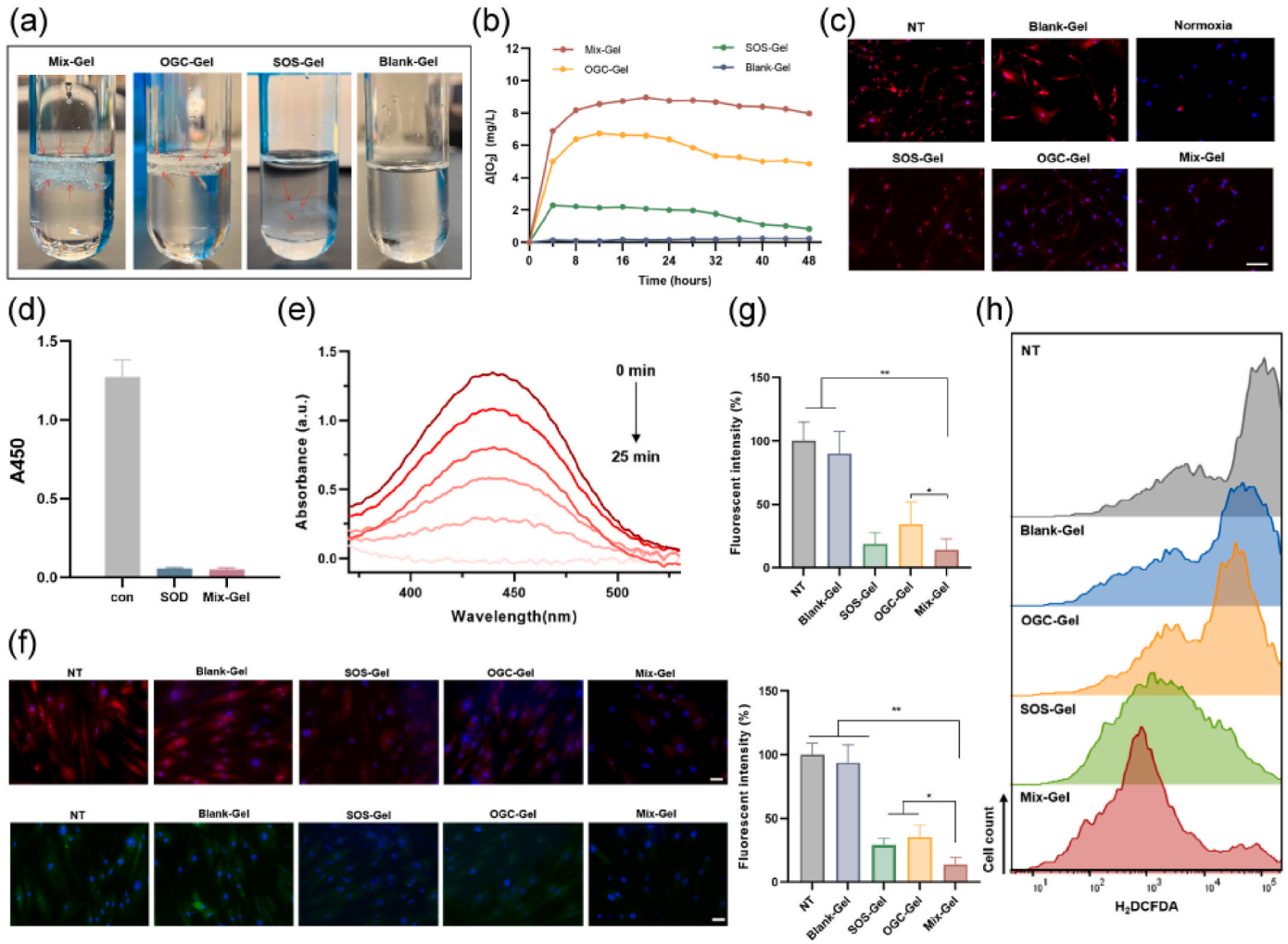

Fig. 3. Evaluation of oxygen production and ROS scavenging. (a) Digital image of oxygen generation from different hydrogels. Red arrows: oxygen bubbles. (b) Oxygen concentration curve of different hydrogels in 48 h. (c) Intracellular hypoxia levels of different treatments characterized by hypoxia indicator, RDPP. Scale bar = 100 μm. (d) Absorbance at 450 nm after 25 min of reaction. (e) UV–vis absorption tested every 5 min throughout 25 min of reaction. (f) Representative SOD (red) and ROS (green) fluorescence images under various treatments. Scale bar = 50 μm. (g) Quantitative assessment of SOD (upper) and ROS (lower) fluorescence intensity (n = 3, mean ± SD). (h) Flow cytometry analysis of H_2DCFDA staining on HDFa cells.

was employed to investigate the therapeutic effectiveness of the hydrogel dressings. The surgical process, application of dressings, and the timeline of the healing process are visually depicted in Fig. 6a. The wound closure progression was closely monitored over the 14-day treatment period. In each experimental group, a notable decrease in the wound area was observed, attributable to epidermal migration (Fig. 6b). The simulated wound healing progression over the time interval was represented in Fig. 6c. Aligning with our in vitro findings, the Mix-Gel treatment exhibited the highest rate of wound closure (Fig. 6e). The quantitative wound area was measured and depicted in Fig. 6d. Notably, infection and inflammation were observed in the Tegaderm and Blank-Gel groups at days 4 and 6, whereas no macroscopic infection was presented in the other treatments. Furthermore, by day 14, the Mix-Gel group demonstrated the most favorable recovery outcome, characterized by scarless healing. In contrast, the other groups displayed noticeable residual wound areas or keloids, which could potentially compromise the restored tissue's normal functionality. A decline in body weight was evident in the first two days following surgery, which can be attributed to the recuperation from anesthesia (Fig. 6f). Overall, the Mix-Gel proved effective in expediting surgical wound healing without inducing keloid formation, ultimately leading to scarless healing outcomes.

Subsequently, a thorough evaluation of the therapeutic efficacy of various treatments was conducted with the wound tissue obtained on day 14. Histopathological examination utilized staining with hematoxylin and eosin (H&E) and Masson's trichrome (Fig. 7a and b). The results on Day 14 revealed that while all treatment groups exhibited wound closure and the development of newly formed epidermis, the Mix-Gel group demonstrated notably flatter wound surfaces, indicative of a continuous and coherent epidermis, which underscores the substantial potential of Mix-Gel in preventing keloid formation and promoting scarless wound healing. Additionally, the Mix-Gel-treated group manifested diminished regions of inflammation and heightened density of newly developed vascular structures, which can be attributed to its cascade enzymatic reaction-mediated ROS scavenging ability and the subsequent production and release of oxygen.

An array of quantitative analysis was performed to assess skin repair parameters, which encompassed various factors such as hair follicle and gland count, scar index, dermal thickness, epidermal thickness, and collagen fraction [40,41]. The Scar Index (SI), a measure of scar size, was determined by dividing the scar area (mm^2) by the average dermal thickness (mm). Our results suggested that the group treated with Mix-Gel exhibited the lowest scar index, suggesting a more positive result of wound healing (Fig. 7c). Measurements of dermal thickness indicated that the Mix-Gel-treated group had a thicker dermal layer, signifying effective tissue repair (Fig. 7d). In contrast, the thickness of

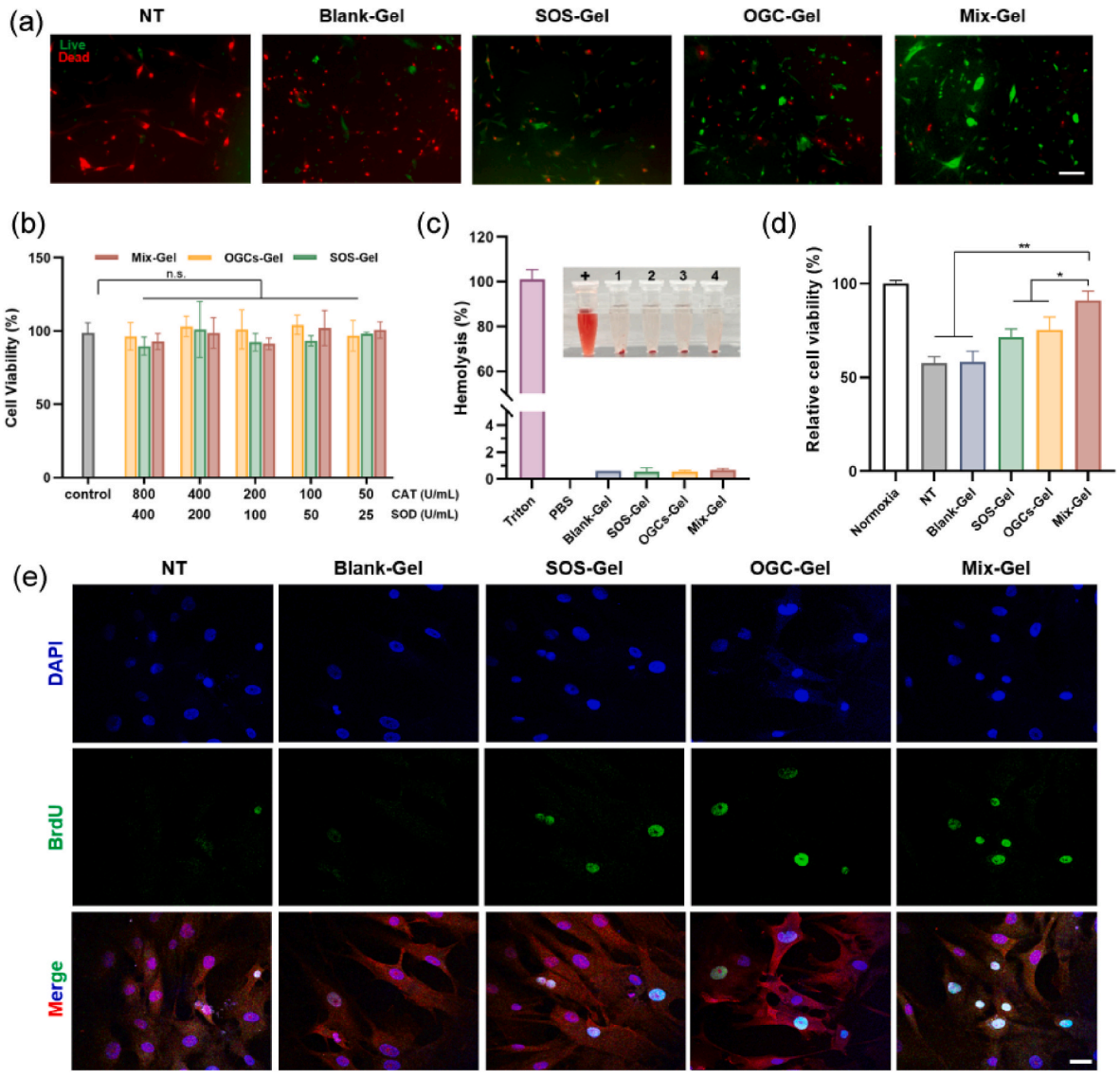

Fig. 4. Assessment of biocompatibility and augmented cell proliferation. (a) Representative fluorescent images of live/dead staining of HDFa cells. Scale bar = 50 μm. (b) Cell toxicity of HDFa cells with different concentrations of Mix-Gel, OGC-Gel, and SOS-Gel treatments (n = 3, mean ± SD). (c) Hemolysis ratio of various treatments and photo of hemolysis (n = 3, mean ± SD). +: Triton; 1: Blank-Gel; 2: SOS-Gel; 3: OGC-Gel; 4: Mix-Gel. (d) Cell proliferation analysis after 24 h of hypoxia incubation (n = 3, mean ± SD). (e) Immunofluorescence images of BrdU incorporation staining of HDFa cells. Scale bar = 50 μm.

the newly formed epidermis closely resembled that of normal skin tissue, indicating a well-balanced and suitable healing response, which can help prevent the development of functionally and aesthetically problematic keloid scars (Fig. 7e). Additionally, the heightened number of newly formed hair follicles (Fig. S15) and glands (Fig. S16) underscores the exceptional quality of healing facilitated by Mix-Gel treatment. Moreover, Masson's trichrome staining revealed that in the Tegaderm and Blank-Gel groups, the collagen bundles exhibited increased thickness, irregular morphology, and a densely packed and disorganized arrangement (Fig. 7b). While augmented collagen thickness contributes to skin firmness, it concurrently has the potential to increase skin stiffness and scar formation [42,43]. Conversely, in the Mix-Gel treated group, there was a substantial presence of collagen fibers exhibiting a more mature phenotype characterized by highly organized alignment, and collagen fiber bundles displayed a thinner profile, with a more loosely organized and regular arrangement, closely resembling the collagen architecture observed in unwounded skin tissue (Fig. S17). The quantitative evaluation of collagen volume fraction corroborated the observed results, confirming the enhanced capability of Mix-Gel to deposit collagen (Fig. 7f).

To further confirm the multifunctional effects of Mix-Gel on angiogenesis, anti-inflammation, and hypoxia alleviation in vivo, we conducted tissue fluorescent staining on the wound tissues at day 14 post-surgery. Adequate oxygen supply is known to be crucial for the regeneration of new blood vessels during wound healing [44]. The results of immunofluorescent staining for CD31, a marker for angiogenesis, exhibited increased expression and fluorescence intensity in the Mix-Gel treated group, highlighting the Mix-Gel's ability to promote angiogenesis (Fig. 8a and b). Furthermore, in line with the hypoxia mitigation observed in HDFa cells, there was a notable reduction in HIF-1α expression in the Mix-Gel group, indicating its effectiveness in alleviating hypoxia within wounds (Fig. 8a and d).

The cascade enzymatic reaction within the nano oxygen chamber aims to mitigate excessive ROS and inflammation, thereby preventing the formation of dysfunctional scars during the healing process. Consequently, we evaluated ROS levels and the macrophage phenotype. Dihydroethidium (DHE) was employed as a widely used probe for detecting cytosolic superoxide and ROS, producing a red fluorescent product, 2-hydroxyethidium, upon reacting with the superoxide anion [45]. DHE staining results on wound tissues revealed significantly lower

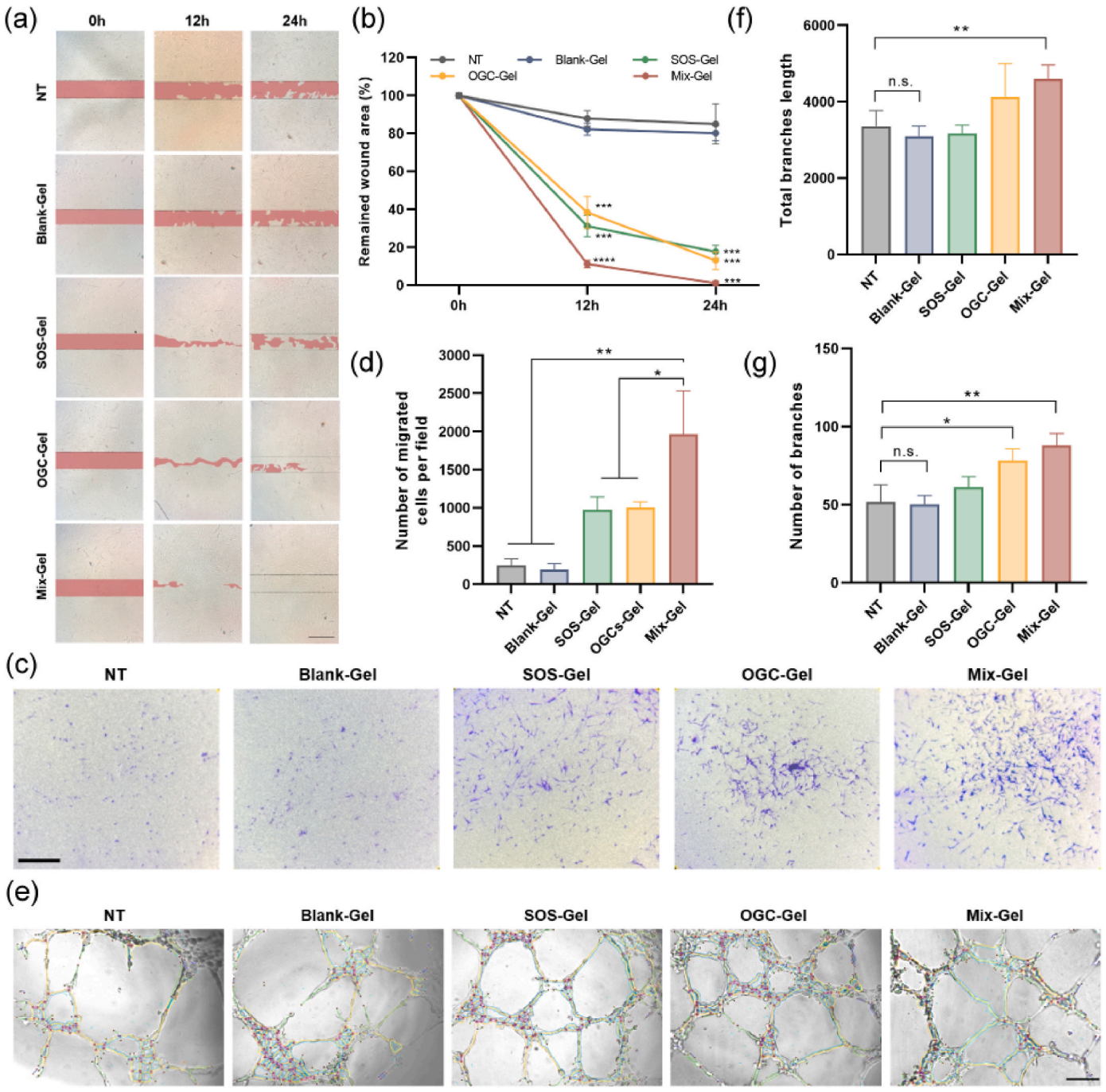

Fig. 5. Evaluation of in vitro cell migration and angiogenesis. (a) Scratch assay for wound healing assessment at 12 h and 24 h after different treatments under hypoxia. Scale bar = 200 μm. (b) Remained wound area percentage of different treatments in (a) (n = 3, mean ± SD). (c) and (d) Microscopic images under brightfield and corresponding quantification of transwell migration assays conducted on HDF-a cells (n = 3, mean ± SD). Scale bar = 200 μm. (e) Evaluation of tube formation capacity in HUVECs following various treatments. Scale bar = 200 μm. Quantitative assessment of (f) total branch length and (g) branch count (n = 3, mean ± SD).

ROS levels in wounds treated with Mix-Gel compared to those treated with Blank-Gel and the Tegaderm control (Fig. 8a and c). The notably high DHE intensity in the Tegaderm control and Blank-Gel groups indicate sustained high ROS levels in healed tissue even after 14 days of treatments, potentially contributing to hypertrophic scar formation. Immunofluorescent staining for CD206 and F4/80, indicative of M2 anti-inflammatory macrophages and a universal marker for macrophages, respectively, was conducted to further assess inflammation levels of various treatments (Fig. 8a and e). Consistent with the in vitro results, Mix-Gel exhibited the highest CD206 expression compared to control groups, affirming its effective anti-inflammatory capacity.

2.6. In vivo wound healing efficacy on porcine full-thickness wound model: pilot study

Porcine full-thickness wound model was further utilized to explore the clinical translation potential of human wound healing. The pig model has gained prominence in wound healing research due to its resemblance to humans in terms of anatomy, physiology, and immune response [46]. Unlike rodents, pig skin closely mirrors human skin

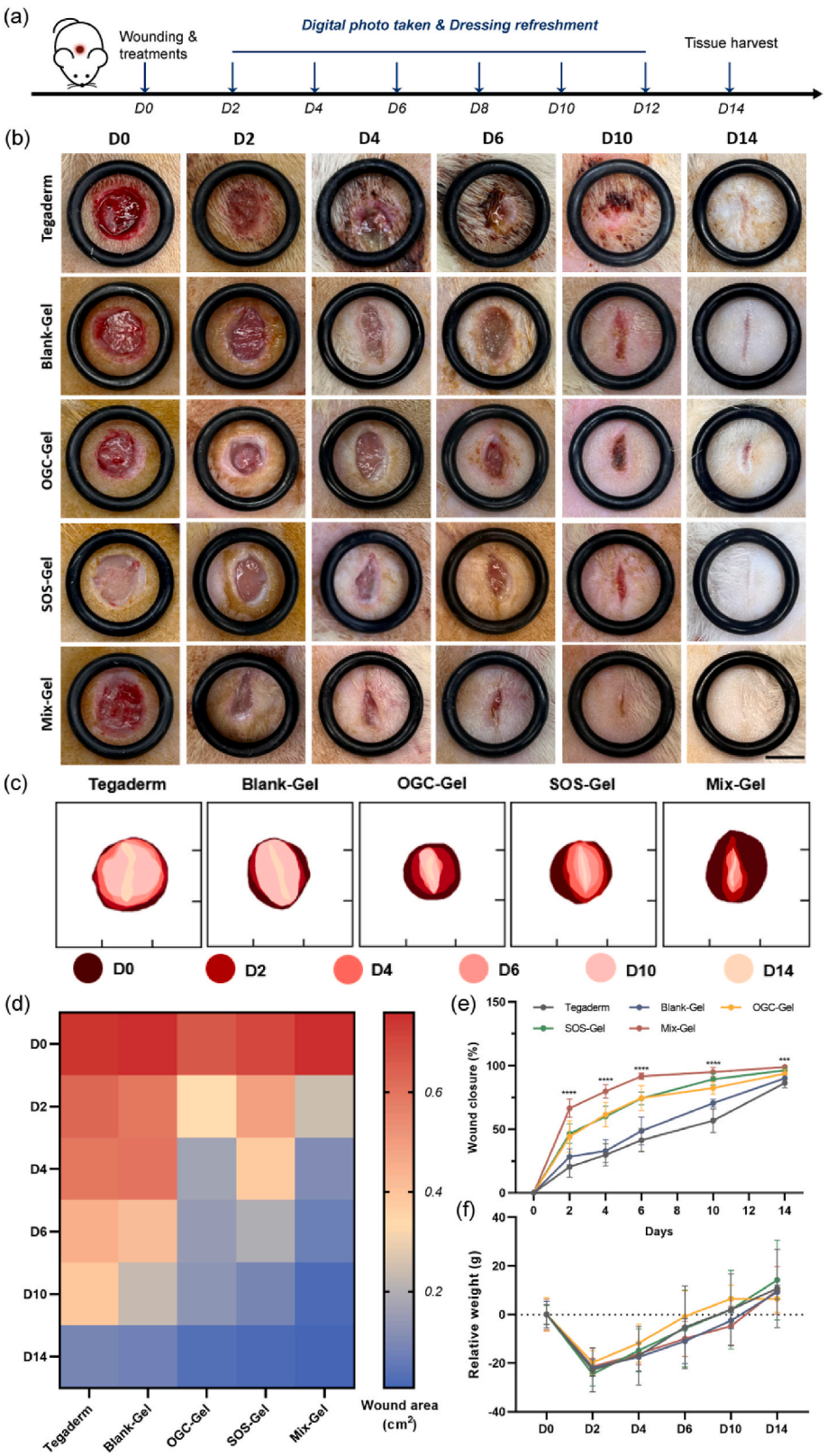

Fig. 6. In vivo wound healing assessment of Mix-Gel on a rat full-thickness wound model. (a) Illustration of wound surgery and treatment timeline. (b) Representative digital photos of wounds with different treatments from D0 to D14. Scale bar = 7 mm. (c) Simulated wound healing process of (b) at different time points. (d) Quantification of wound area (cm^2) at different treatments over the period of 14 days. (e) Wound closure rate of different treatments from D0 to D14 (n = 6/group, mean ± SD). (f) Relative body weight of rats over time.

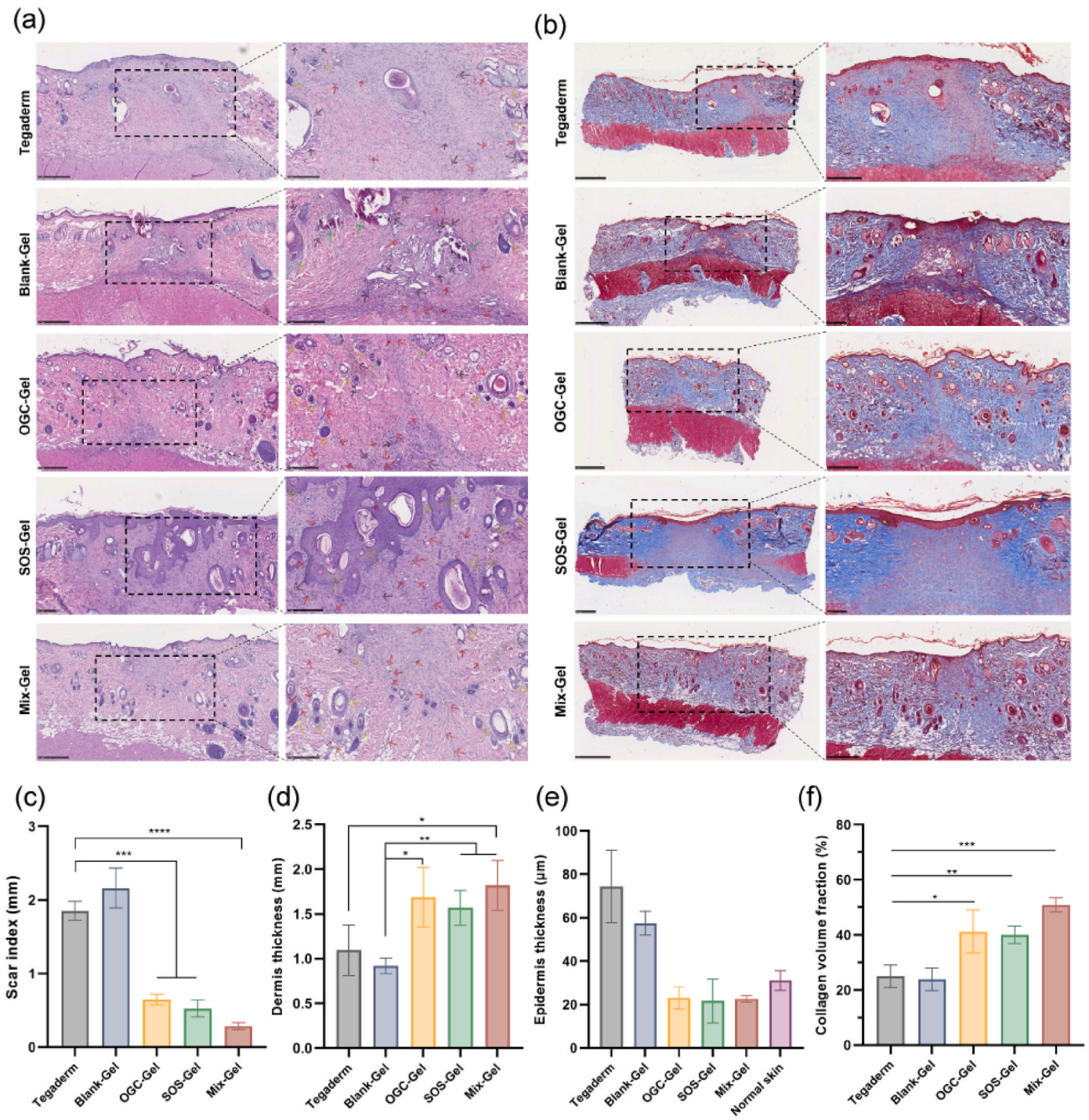

Fig. 7. Histopathological assessment of wound tissue treated with hydrogels. (a) H&E and (b) Masson's trichrome staining images of wound tissue collected at D14. The arrows represent: blood clots (green), inflammation (black), newly formed blood vessels (red), newly formed hair follicles (yellow). Quantitative analysis of (c) Scar index, (d) Dermis thickness, (e) Epidermis thickness, and (f) Collagen volume fraction (n = 3, mean ± SD).

architecture given its tight connection to subcutaneous tissue. Studies have shown comparable thickness of skin layers, blood supply in dermis, and dermal-epidermal ratio between pigs and humans [47]. Both species share developed rete-ridges, pars papillaris, and abundant subdermal fatty tissue, with fat serving as the main insulation, which makes the porcine model a suitable candidate for investigating clinical applications [48,49].

In this preliminary investigation, we conducted a comparative analysis of Mix-Gel, OGC-Gel, and Blank-Gel's impact on wound healing at day 3 post-surgery, which corresponds to the initial proliferation stage. We employed two types of wounds: punch and stitch wounds (Fig. 9a). The results demonstrated that Mix-Gel significantly enhanced wound closure rates in both types of wounds (Fig. 9b, c and 9e). This is a crucial factor in early healing, since rapid contraction provides a barrier and prevents microbial invasion. Histological analysis revealed that Mix-Gel-treated wounds exhibited the increased formation of granulation tissue and hair follicles (Fig. 9d and f). Additionally, the epidermis thickness was greater in the Mix-Gel group, indicating an accelerated progression into the proliferation stage of wound healing. The preference for OGC-Gel in stitched wound healing over punched wound

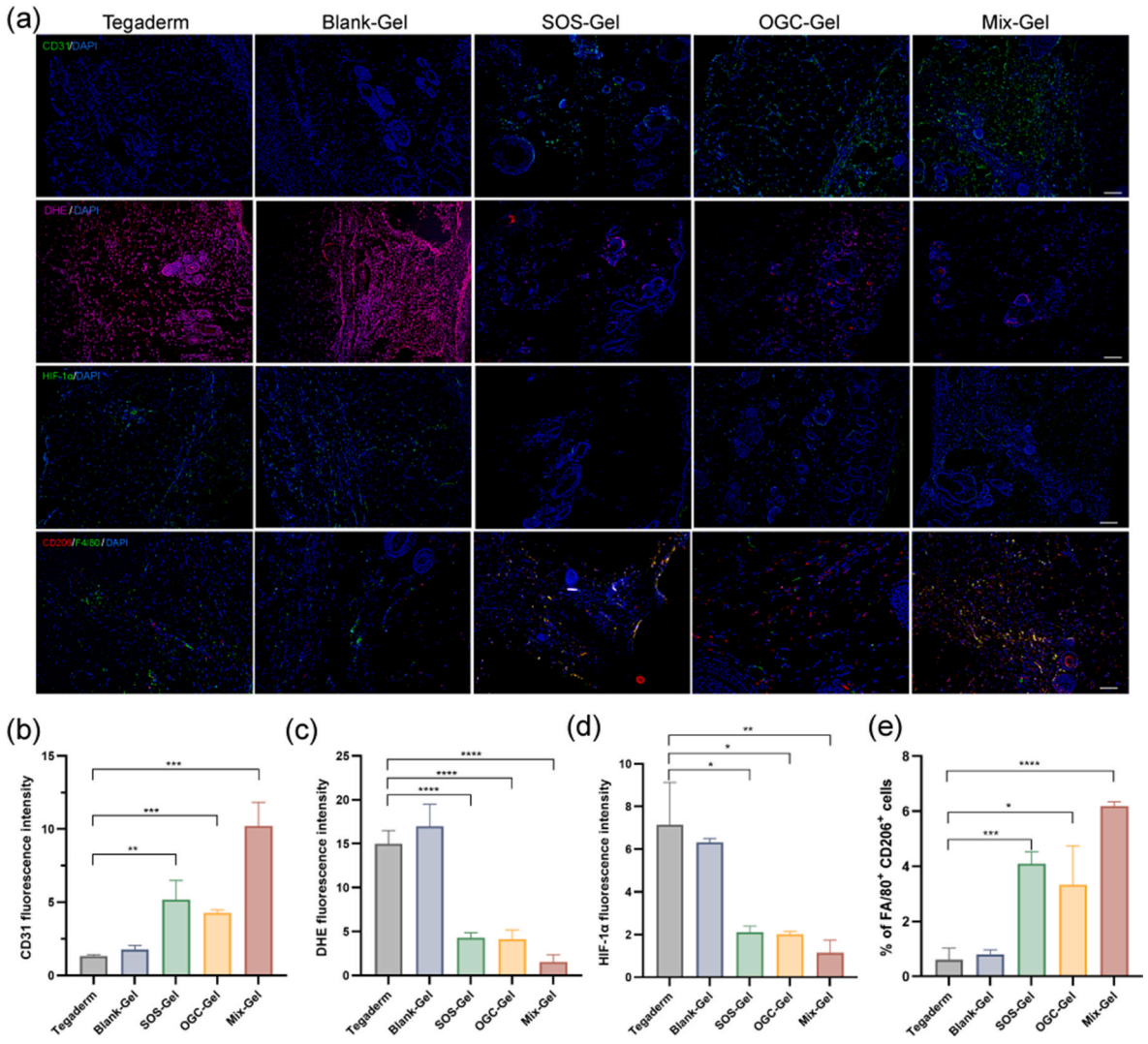

Fig. 8. Evaluation of in vivo angiogenesis, ROS level, hypoxia mitigation, and macrophage phenotype. (a) Wound tissue fluorescent staining. Row 1: Immunofluorescent staining of CD31 on day 14 post treatment. Scale bar = 200 μm. Row 2: DHE staining for the examination of ROS levels on day 14. Scale bar = 200 μm. Row 3: Immunofluorescent staining of HIF-1α on day 14. Scale bar = 200 μm. Row 4: Immunofluorescent staining of M2 phenotype macrophage (CD206, red) and F4/80 (green) Scale bar = 100 μm. Quantification of fluorescent intensity of (b) CD31; (c) DHE; (d) HIF-1α (n = 3, mean ± SD). (e) Quantification of the percentage of M2 macrophages (n = 3, mean ± SD).

healing can be attributed to several factors. An important factor to consider is that sutured wounds, where closure is achieved using sutures, typically exhibit a smoother and more structurally sound surface. This smoother surface promotes enhanced adherence of OGC-Gel, consequently improving its capacity to deliver oxygen to the wound site. The inherently even and tightly sealed nature of sutured wounds offers a more favorable environment for the successful application of the gel. In summary, despite the inability of punched wounds to offer a fully sealed environment, Mix-Gel exhibited significant and essential wound healing efficacy, underscoring its potential for clinical applications.

3. Discussion

The development of advanced wound healing strategies hold significant promise for improving patient outcomes and reducing the burden of wound care patients. In this study, we investigated the potential of Mix-Gel, a cascade enzymatic reaction-based oxygen generating nanocarriers laden hydrogel, as a therapeutic means to enhance acute wound healing. The incorporation of two enzyme-based oxygen nanobubbles, SOS and OGC, endowed the hydrogel with antioxidant and oxygen-supplying capabilities. Through the scavenging actions of SOS and OGC, superoxide anion and H_2O_2 were effectively eliminated while generating oxygen. Furthermore, the oxygen released from the nanobubbles synergistically contributed to the alleviation of hypoxia, as evidenced by the observed effects on HDFa cells.

Our results highlight several important aspects of Mix-Gel's effectiveness in promoting wound closure and tissue regeneration. One of the key observations was the enhanced wound closure rate associated with Mix-Gel application in both rat and porcine full-thickness wound model, as early wound contraction not only contributes to tissue protection but also prevents the invasion of microorganisms, thereby minimizing the risk of infection. The rapid wound closure, hypoxia mitigation, and anti-inflammation function was essential to obtain scarless wound healing and reduce the formation of keloids, which underscores the potential clinical applications of Mix-Gel. While our nano oxygen chamber effectively mitigates excessive ROS and prevents scarring, the system as such is not applicable for infected wounds. Future research will explore incorporating antibacterial materials for broader applications. Although our study showed promise, wound tensile strength was not assessed due to physiological differences between rodents and humans, and hence requires further investigation in porcine models.

In conclusion, our study provides compelling evidence for the

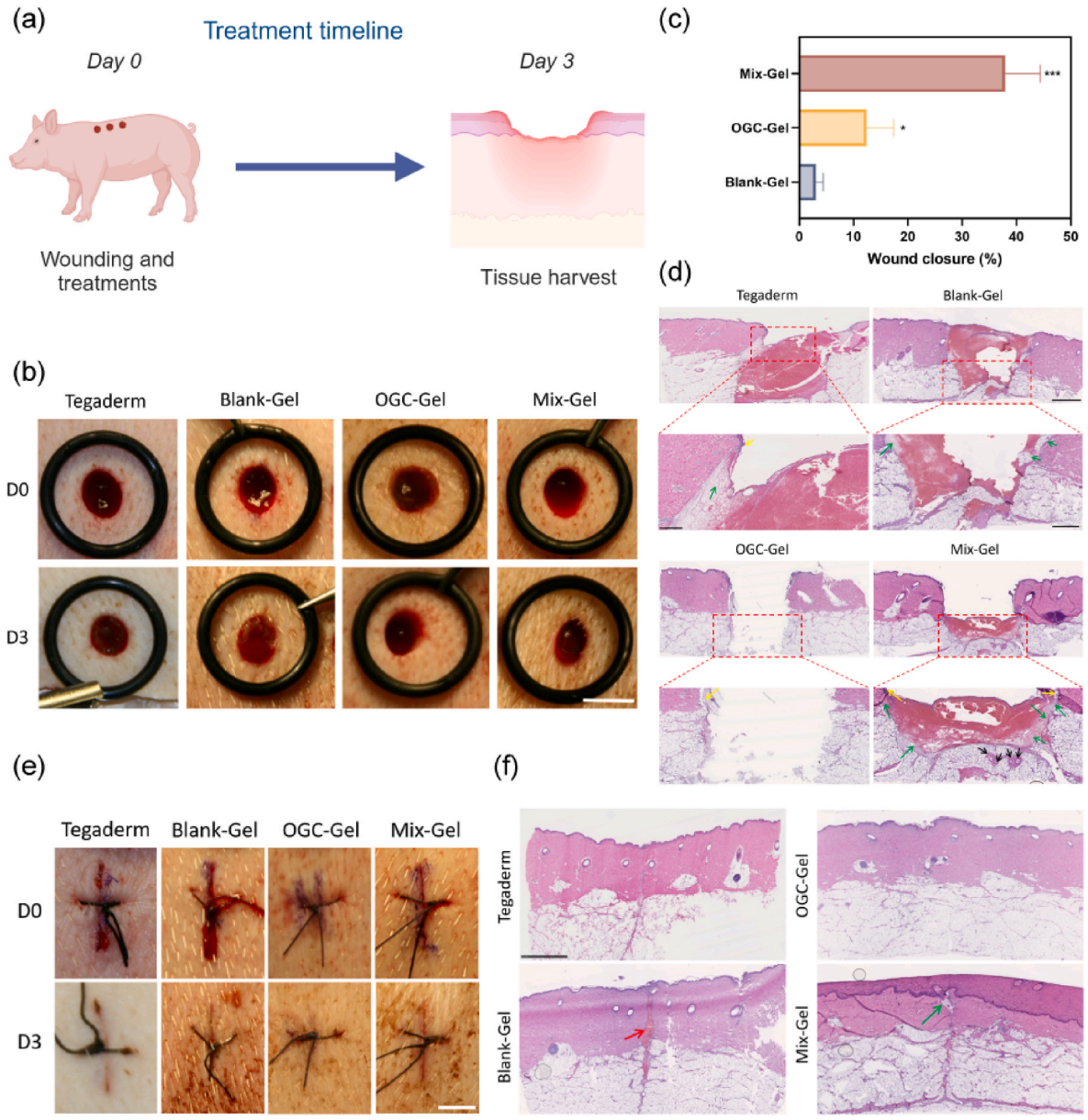

Fig. 9. In vivo wound healing assessment of Mix-Gel on a porcine full-thickness wound model. (a) Illustration of the wound models (2 patterns: punch and stitch wounds) and treatment timeline. Illustration was created with BioRender.com. (b) Representative digital photos of wounds with varied treatments at different time points. Scale bar = 7 mm (The Tegaderm group data is shared with reference [49]). (c) Wound closure rate (n = 3/group, mean ± SD) over time. (d) Representative H&E imaging of punch wound tissue on Day 3. Yellow arrow: newly generated epidermis; Green arrow: granulation tissue; Black arrow: newly born glands. (e) Representative digital images of wounds with varied treatments at different time points. Scale bar = 7 mm. (f) Representative images of H&E imaging of stitch wound tissue on Day 3. Red arrow: blood clot; Green arrow: newly generated granulation tissue.

effectiveness of Mix-Gel in mitigating hypoxia, scavenging ROS, promoting wound closure and tissue regeneration. The observed improvements in wound closure rates and histological features in rat and porcine models suggest that Mix-Gel holds significant promise as an advanced wound healing strategy. The cascade enzymatic reaction-mediated hypoxia relief and antioxidant property positions Mix-Gel as a potentially valuable wound care treatment. Further investigations and clinical trials are warranted to validate its efficacy across a broader range of wound scenarios and to establish its safety and effectiveness in a clinical setting.

4. Experimental section

4.1. Preparation of SOS and SOS-con

8 mg of SOD and 16 mg of dextran sulfate were dissolved in 4 mL sterile 1 × PBS buffer (pH = 7.4), and then fully mixed using a magnetic stirrer overnight. Subsequently, the ultrasonication was carried out on ice bath utilizing an ultrasonic cell disruptor (SFX250, Branson, USA). Ultrasonication was performed in a cyclic pattern of 3 s on and 3 s off, at an amplitude of 60 %, for a duration of 5 min. Throughout the ultrasonication process, a continuous supply of oxygen with a flow rate of 0.45 L/min was introduced into the system to form SOS. The fabrication process of SOS-con involved utilizing an identical concentration of SOD and dextran sulfate as employed in the case of SOS. After a thorough overnight mixing, ultrasonication was performed using the same

conditions as the SOS fabrication process, except nitrogen was used in place of oxygen. The flow rate of nitrogen during this step was maintained at 0.45 L/min. This modification in the gas environment during ultrasonication serves as the distinctive factor in the fabrication process, differentiating SOS-con from SOS. The resultant solution was subjected to filtration using a 0.22 μm cellulose acetate filter. To remove the unreacted SOD, the final step involved an ultrafiltration process using an Amicon Ultra 15 filter with a molecular weight cutoff of 100 kDa.

4.2. Characterization of SOS

The hydrodynamic size distribution, zeta potential, TEM images, SEM images, UV–Vis absorbance, particle concentration, diameter stability at 4 °C, SOD activity, SOD conjugation efficiency, and FT-IR spectrum of SOS nanoparticle was measured. All detailed procedures were included in the Supporting Information.

4.3. Oxygen generation capacity, superoxide elimination and ROS scavenging evaluation

Oxygen generation and release for a period of 6 h was investigated. The absorbance at 450 nm was tested to verify superoxide elimination. SO and ROS detection after treated hydrogels was examined by ROS/SOD fluorescence detection kit. Detailed procedures can be found in the Supporting Information.

4.4. Preparation and characteristics of hydrogels

To form SOS-Gel and OGC-Gel, 250 μL SOS or OGC was fully mixed with 250 μL PBS and 500 μL sodium alginate (2 wt%), respectively. For Mix-Gel, 250 μL SOS and 250 μL OGC was added into 500 μL sodium alginate (2 wt%) and thoroughly blended. Finally, 100 μL of 0.1 M $CaCl_2$ was introduced into the mixture, and the resulting solution was allowed to undergo a gelation process for 3 min.

ESEM (FEI Quanta FEG 450 ESEM) was utilized to observe the microstructure of hydrogels. The rheological behaviors of different hydrogels were measured by rheometer. All detailed procedures were included in the Supporting Information.

4.5. Cell viability, hemolysis assay, and cell proliferation assay

The assessment of cell viability was performed utilizing HEKa cells and HDFa cells, following the documented methodology. The hemolysis assay was conducted utilizing red blood cells from rats, following the established protocol as previously reported. Cell proliferation assay was conducted on HDFa cells, according to the previously reported method. All detailed procedures were included in the Supporting Information.

4.6. Scratching assay

HDF-a cells were initially pre-seeded within a 24-well plate. Once the confluency of cells reached 80%–90 %, controlled scratch wounds were made using a sterile 200 μL pipette tip. Subsequently, the culture medium was substituted with DMEM supplemented with 1 % FBS. The hydrogels were then added to the upper chamber of cell culture inserts (Millicell®, Sigma-Aldrich), and the entire system was placed within a hypoxia chamber, maintained under the specified hypoxic conditions. Over various time intervals (12 h and 24 h), healing was observed via microscopy (ZEISS) and quantified using the ImageJ software.

4.7. Transwell migration assay

In the transwell migration assay, HDF-a cells were seeded within the upper chamber of cell culture inserts at a density of 1×10^4 cells/mL. Simultaneously, hydrogels were added into the lower chamber, containing the culture medium. Following a 24-h incubation period, cells situated on the upper side of the insert were gently eliminated using a cotton swab. Subsequently, the cells that had migrated to the lower side of the insert were stained with a 0.5 % crystal violet solution for 1 h. The quantification of the migrated cell population was performed using the ImageJ software.

4.8. Tube formation assay

In the tube formation assay, HUVEC cells at a passage earlier than the 6th were employed for evaluation. Specifically, 100 μL of Matrigel (Corning) was introduced into each well of a 96-well plate and subsequently incubated at 37 °C to solidify for a duration of 1 h. Following this, 10,000 HUVECs were seeded into each well, after which different hydrogels were treated. The plates were then placed within a hypoxia chamber enriched hypoxic mixture as described. After 6-h of incubation, brightfield images capturing the formation of tubular structures were acquired using a Leica microscope. Images of tube formation assay were analyzed and processed with Angiogenesis Analyzer in ImageJ (National Institute of Health, Bethesda, MD, USA). Angiogenesis Analyzer extracts the characteristics of the tube network and provides output including color coding and the number of tubes and branches, hence, it is broadly used in quantitative assessment of angiogenesis. For this work, we did 3 replicates and quantified the number of branches and total branch length, which are the most representative parameters of angiogenesis.

4.9. In vivo rat wound healing study

All animal studies were performed in accordance with the guidelines of the Institutional Animal Care and Use Committee and the Division of Animal Resources at the University of Illinois (IACUC Protocol#: 23,012). Male Sprague-Dawley rats, aged 8 weeks and weighing 250–300 g, were sourced from Envigo Laboratory (Indianapolis, IN) for the study. The rats were allocated randomly into five groups: NT, Blank-Gel, OGC-Gel, SOS-Gel, and Mix-Gel. Full-thickness wounds were meticulously created on the dorsal area using a sterile disposable 8 mm diameter dermal biopsy punch (MEDLINE) [50]. These wounds extended to a depth of 2 mm. The hydrogels were applied to the wounds and refreshed on a bi-daily basis post-surgery. The progression of wound closure within 14 days was monitored using a digital camera. Subsequently, the determination of wound closure areas was executed utilizing Image J software. The wound closure rate (%) at various time points was computed according to the formula:

$$\text{Wound closure } (\%) = [(\text{Area } (0 \text{ day}) - \text{Area } (\text{n day}))/\text{Area } (0 \text{ day})] \times 100\ \%,$$

wherein “n" denotes the post-surgery treatment day.

After 14 days had elapsed, the animals were humanely euthanized, and the wound tissues were extracted for analysis. Subsequently, the tissues were subjected to fixation using a 10 % formalin neutral buffered solution (Sigma-Aldrich) for further H&E and Masson Trichrome staining. The histology images were captured using a microscope.

4.10. In vivo porcine wound healing pilot study

All animal studies were performed in accordance with the guidelines of the Institutional Animal Care and Use Committee and the Division of Animal Resources at the University of Illinois (IACUC Protocol#: 22,133). The detailed procedures were provided in the Supporting Information.

4.11. Statistical analysis

Statistical significance tests were conducted using a two-tailed Student’s t-test for pairwise comparisons between two groups, and one-way analysis of variance (ANOVA) was used for comparisons among multiple groups. A significance level of $p < 0.05$ was considered statistically

significant. *: $p < 0.05$, **: $p < 0.01$, ***: $p < 0.001$, and ****: $p < 0.0001$.

CRediT authorship contribution statement

Xiaoxue Han: Writing – original draft, Methodology, Investigation, Formal analysis, Data curation, Conceptualization. **Leah Ju:** Writing – review & editing, Methodology. **Chai Saengow:** Data curation, Formal analysis, Methodology, Writing – review & editing. **Wen Ren:** Writing – original draft, Methodology, Formal analysis. **Randy Ewoldt:** Data curation, Formal analysis, Methodology, Visualization, Writing – review & editing. **Timothy Fan:** Writing – review & editing, Methodology. **Joseph Irudayaraj:** Writing – review & editing, Supervision, Resources, Project administration, Funding acquisition, Conceptualization.

Declaration of competing interest

The authors declare that they have no known competing financial interests or personal relationships that could have appeared to influence the work reported in this paper.

Acknowledgement

The authors graciously acknowledge support from the Cancer Scholars Program for XH, a Carle Foundation Hospital and Cancer Center at Illinois initiative. Partial funding from the Health Maker Lab of the Carle Illinois College of Medicine and the Mikashi Award from the Institute of Genomic Biology, University of Illinois at Urbana-Champaign is greatly appreciated. Thanks to Dr. Harley for providing us with the HUVEC cell line. We thank the TEP at Cancer Center at Illinois (UIUC) for assistance in biological evaluation. Our sincere thanks to Karen Doty at the Histology facility in the Department of Comparative Biosciences for the assistance in tissue processing and immunofluorescent staining. We thank Zunaira Shoaib for assistance in tissue analysis. Thanks to Dr. Tor Jensen for assistance in the animal studies.

Appendix A. Supplementary data

Supplementary data to this article can be found online at https://doi.org/10.1016/j.bioactmat.2024.01.010.

☐The authors declare the following conflict of interest relating to the work reported in this paper:

References

[1] A.J. Singer, R.A.F. Clark, Cutaneous wound healing, N. Engl. J. Med. 341 (10) (1999) 738–746, https://doi.org/10.1056/NEJM199909023411006.
[2] N.B. Menke, K.R. Ward, T.M. Witten, D.G. Bonchev, R.F. Diegelmann, Impaired wound healing, Clin. Dermatol. 25 (1) (2007) 19–25, https://doi.org/10.1016/j.clindermatol.2006.12.005.
[3] F.B. Niessen, P.H.M. Spauwen, J. Schalkwijk, M. Kon, On the nature of hypertrophic scars and keloids: a review, Plast. Reconstr. Surg. 104 (5) (1999).
[4] D. Wolfram, A. Tzankov, P. Pülzl, H. Piza-Katzer, Hypertrophic scars and keloids—a review of their pathophysiology, risk factors, and therapeutic management, Dermatol. Surg. 35 (2) (2009) 171–181, https://doi.org/10.1111/j.1524-4725.2008.34406.x.
[5] M. Takeo, W. Lee, M. Ito, Wound healing and skin regeneration, Cold Spring Harb. Perspect. Med. 5 (1) (2015).
[6] R. Ogawa, Keloid and hypertrophic scars are the result of chronic inflammation in the reticular dermis, Int. J. Mol. Sci. 18 (2017).
[7] Y. Xiong, X. Chu, T. Yu, S. Knoedler, A. Schroeter, L. Lu, K. Zha, Z. Lin, D. Jiang, Y. Rinkevich, et al., Reactive oxygen species-scavenging nanosystems in the treatment of diabetic wounds, n/a (n/a), Adv. Healthcare Mater. (2023) 2300779, https://doi.org/10.1002/adhm.202300779.
[8] Z.-C. Wang, W.-Y. Zhao, Y. Cao, Y.-Q. Liu, Q. Sun, P. Shi, J.-Q. Cai, X.Z. Shen, W.-Q. Tan, The roles of inflammation in keloid and hypertrophic scars, Front. Immunol. (2020) 11, https://doi.org/10.3389/fimmu.2020.603187.
[9] R. Tanaka, Y. Umeyama, H. Hagiwara, R. Ito-Hirano, S. Fujimura, H. Mizuno, R. Ogawa, Keloid patients have higher peripheral blood endothelial progenitor cell counts and CD34+ cells with normal vasculogenic and angiogenic function that overexpress vascular endothelial growth factor and interleukin-8, Int. J. Dermatol. 58 (12) (2019) 1398–1405, https://doi.org/10.1111/ijd.14575.
[10] X. Han, L.S. Ju, J. Irudayaraj, Oxygenated wound dressings for hypoxia mitigation and enhanced wound healing, Mol. Pharm. 20 (7) (2023) 3338–3355, https://doi.org/10.1021/acs.molpharmaceut.3c00352.
[11] J. Wu, X. Wang, Q. Wang, Z. Lou, S. Li, Y. Zhu, L. Qin, H. Wei, Nanomaterials with enzyme-like characteristics (nanozymes): next-generation artificial enzymes (II), Chem. Soc. Rev. 48 (4) (2019) 1004–1076.
[12] H. Wang, K. Wan, X. Shi, Recent advances in nanozyme research, Adv. Mater. 31 (45) (2019) 1805368, https://doi.org/10.1002/adma.201805368.
[13] X. Mou, Q. Wu, Z. Zhang, Y. Liu, J. Zhang, C. Zhang, X. Chen, K. Fan, H. Liu, Nanozymes for regenerative medicine, Small Methods 6 (11) (2022) 2200997, https://doi.org/10.1002/smtd.202200997.
[14] Y. Li, R. Fu, Z. Duan, C. Zhu, D. Fan, Artificial nonenzymatic antioxidant MXene nanosheet-anchored injectable hydrogel as a mild photothermal-controlled oxygen release platform for diabetic wound healing, ACS Nano 16 (5) (2022) 7486–7502, https://doi.org/10.1021/acsnano.1c10575.
[15] G.H.J. de Smet, L.F. Kroese, A.G. Menon, J. Jeekel, A.W.J. van Pelt, G.-J. Kleinrensink, J.F. Lange, Oxygen therapies and their effects on wound healing, Wound Repair Regen. 25 (4) (2017) 591–608, https://doi.org/10.1111/wrr.12561.
[16] L.K. Kalliainen, G.M. Gordillo, R. Schlanger, C.K. Sen, Topical oxygen as an adjunct to wound healing: a clinical case series, Pathophysiology 9 (2) (2003) 81–87, https://doi.org/10.1016/S0928-4680(02)00079-2.
[17] M.A. Howard, R. Asmis, K.K. Evans, T.A. Mustoe, Oxygen and wound care: a review of current therapeutic modalities and future direction, Wound Repair Regen. 21 (4) (2013) 503–511, https://doi.org/10.1111/wrr.12069.
[18] M. Heyboer, D. Sharma, W. Santiago, N. McCulloch, Hyperbaric oxygen therapy: side effects defined and quantified, Adv. Wound Care 6 (6) (2017) 210–224, https://doi.org/10.1089/wound.2016.0718.
[19] W. Jiang, X. Han, T. Zhang, D. Xie, H. Zhang, Y. Hu, An oxygen self-evolving, multistage delivery system for deeply located hypoxic tumor treatment, Adv. Healthcare Mater. 9 (2) (2020) 1901303, https://doi.org/10.1002/adhm.201901303.
[20] L.R. Sayadi, D.A. Banyard, M.E. Ziegler, Z. Obagi, J. Prussak, M.J. Klopfer, G.R. D. Evans, A.D. Widgerow, Topical oxygen therapy & micro/nanobubbles: a new modality for tissue oxygen delivery, Int. Wound J. 15 (3) (2018) 363–374, https://doi.org/10.1111/iwj.12873.
[21] P. Bhandari, X. Wang, J. Irudayaraj, Oxygen nanobubble tracking by light scattering in single cells and tissues, ACS Nano 11 (3) (2017) 2682–2688, https://doi.org/10.1021/acsnano.6b07478.
[22] D.V.B. Batchelor, F.J. Armistead, N. Ingram, S.A. Peyman, J.R. McLaughlan, P. L. Coletta, S.D. Evans, Nanobubbles for therapeutic delivery: production, stability and current prospects, Curr. Opin. Colloid Interface Sci. 54 (2021) 101456, https://doi.org/10.1016/j.cocis.2021.101456.
[23] R. Cavalli, A. Bisazza, A. Rolfo, S. Balbis, D. Madonnaripa, I. Caniggia, C. Guiot, Ultrasound-mediated oxygen delivery from chitosan nanobubbles, Int. J. Pharm. 378 (1) (2009) 215–217, https://doi.org/10.1016/j.ijpharm.2009.05.058.
[24] Z. Li, Y. Zheng, Q. Sun, J. Wang, B. Zheng, Z. Guo, Structural characteristics and emulsifying properties of myofibrillar protein-dextran conjugates induced by ultrasound Maillard reaction, Ultrason. Sonochem. 72 (2021) 105458, https://doi.org/10.1016/j.ultsonch.2020.105458.
[25] S.S. Rohiwal, Z. Ellederova, A.P. Tiwari, M. Alqarni, S.T. Elazab, G. El-Saber Batiha, S.H. Pawar, N.D. Thorat, Self-assembly of bovine serum albumin (BSA)–dextran bio-nanoconjugate: structural, antioxidant and in vitro wound healing studies, RSC Adv. 11 (8) (2021) 4308–4317, https://doi.org/10.1039/D0RA09301G, 10.1039/D0RA09301G.
[26] Ş. Akkuş Çetinus, H. Nursevin Öztop, Immobilization of catalase into chemically crosslinked chitosan beads, Enzym. Microb. Technol. 32 (7) (2003) 889–894, https://doi.org/10.1016/S0141-0229(03)00065-6.
[27] H.-U. Bergmeyer, Methods of Enzymatic Analysis, Elsevier, 2012.
[28] L.A. Schneider, A. Korber, S. Grabbe, J. Dissemond, Influence of pH on wound-healing: a new perspective for wound-therapy? Arch. Dermatol. Res. 298 (9) (2007) 413–420.
[29] X. Han, Y. Jeong, J. Irudayaraj, Nanocatalase-based oxygen-generating nanocarriers for active oxygen delivery to relieve hypoxia in pancreatic cancer, ACS Appl. Nano Mater. 5 (11) (2022) 17248–17257, https://doi.org/10.1021/acsanm.2c04241.
[30] B. Gullón, M.I. Montenegro, A.I. Ruiz-Matute, A. Cardelle-Cobas, N. Corzo, M. E. Pintado, Synthesis, optimization and structural characterization of a chitosan–glucose derivative obtained by the Maillard reaction, Carbohydr. Polym. 137 (2016) 382–389, https://doi.org/10.1016/j.carbpol.2015.10.075.
[31] J.-F. Su, Z. Huang, X.-Y. Yuan, X.-Y. Wang, M. Li, Structure and properties of carboxymethyl cellulose/soy protein isolate blend edible films crosslinked by Maillard reactions, Carbohydr. Polym. 79 (1) (2010) 145–153, https://doi.org/10.1016/j.carbpol.2009.07.035.
[32] L. Sheng, G. Tang, Q. Wang, J. Zou, M. Ma, X. Huang, Molecular characteristics and foaming properties of ovalbumin-pullulan conjugates through the Maillard reaction, Food Hydrocolloids 100 (2020) 105384, https://doi.org/10.1016/j.foodhyd.2019.105384.
[33] A.V. Peskin, C.C. Winterbourn, A microtiter plate assay for superoxide dismutase using a water-soluble tetrazolium salt (WST-1), Clin. Chim. Acta 293 (1) (2000) 157–166, https://doi.org/10.1016/S0009-8981(99)00246-6.
[34] A.S. Tan, M.V. Berridge, Superoxide produced by activated neutrophils efficiently reduces the tetrazolium salt, WST-1 to produce a soluble formazan: a simple colorimetric assay for measuring respiratory burst activation and for screening anti-inflammatory agents, J. Immunol. Methods 238 (1) (2000) 59–68, https://doi.org/10.1016/S0022-1759(00)00156-3.

[35] X. Zhang, D. Yao, W. Zhao, R. Zhang, B. Yu, G. Ma, Y. Li, D. Hao, F.-J. Xu, Engineering platelet-rich plasma based dual-network hydrogel as a bioactive wound dressing with potential clinical translational value, Adv. Funct. Mater. 31 (8) (2021) 2009258, https://doi.org/10.1002/adfm.202009258.
[36] P. Rastogi, B. Kandasubramanian, Review of alginate-based hydrogel bioprinting for application in tissue engineering, Biofabrication 11 (4) (2019) 042001, https://doi.org/10.1088/1758-5090/ab331e.
[37] S.M. Hashemnejad, S. Kundu, Rheological properties and failure of alginate hydrogels with ionic and covalent crosslinks, Soft Matter 15 (39) (2019) 7852–7862, https://doi.org/10.1039/C9SM01039D, 10.1039/C9SM01039D.
[38] T. Goyal, C.L. Schmotzer, Validation of hemolysis index thresholds optimizes detection of clinically significant hemolysis, Am. J. Clin. Pathol. 143 (4) (2015) 579–583, https://doi.org/10.1309/AJCPDUDE1HRA0YMR.
[39] G. Lowe, R. Stike, M. Pollack, J. Bosley, P. O'Brien, A. Hake, G. Landis, N. Billings, P. Gordon, S. Manzella, et al., Nursing blood specimen collection techniques and hemolysis rates in an emergency department: analysis of venipuncture versus intravenous catheter collection techniques, J. Emerg. Nurs. 34 (1) (2008) 26–32, https://doi.org/10.1016/j.jen.2007.02.006.
[40] Y. Liang, J. He, B. Guo, Functional hydrogels as wound dressing to enhance wound healing, ACS Nano 15 (8) (2021) 12687–12722, https://doi.org/10.1021/acsnano.1c04206.
[41] C.A.B. Jahoda, A.J. Reynolds, Hair follicle dermal sheath cells: unsung participants in wound healing, Lancet 358 (9291) (2001) 1445–1448, https://doi.org/10.1016/S0140-6736(01)06532-1.
[42] Zhang, X.; Wang, Z.; Jiang, H.; Zeng, H.; An, N.; Liu, B.; Sun, L.; Fan, Z. Self-powered enzyme-linked microneedle patch for scar-prevention healing of diabetic wounds. Sci. Adv. 9 (28), eadh1415. DOI: 10.1126/sciadv.adh1415.
[43] P.D.H.M. Verhaegen, P.P.M. Van Zuijlen, N.M. Pennings, J. Van Marle, F. B. Niessen, C.M.A.M. Van Der Horst, E. Middelkoop, Differences in collagen architecture between keloid, hypertrophic scar, normotrophic scar, and normal skin: an objective histopathological analysis, Wound Repair Regen. 17 (5) (2009) 649–656, https://doi.org/10.1111/j.1524-475X.2009.00533.x.
[44] F. Gottrup, Oxygen in wound healing and infection, World J. Surg. 28 (3) (2004) 312–315, https://doi.org/10.1007/s00268-003-7398-5.
[45] A. Wojtala, M. Bonora, D. Malinska, P. Pinton, J. Duszynski, M.R. Wieckowski, Chapter thirteen - methods to monitor ROS production by fluorescence microscopy and fluorometry, in: L. Galluzzi, G. Kroemer (Eds.), Methods in Enzymology, vol. 542, Academic Press, 2014, pp. 243–262.
[46] A. Summerfield, F. Meurens, M.E. Ricklin, The immunology of the porcine skin and its value as a model for human skin, Mol. Immunol. 66 (1) (2015) 14–21, https://doi.org/10.1016/j.molimm.2014.10.023.
[47] U. Jacobi, M. Kaiser, R. Toll, S. Mangelsdorf, H. Audring, N. Otberg, W. Sterry, J. Lademann, Porcine ear skin: an in vitro model for human skin, Skin Res. Technol. 13 (1) (2007) 19–24, https://doi.org/10.1111/j.1600-0846.2006.00179.x.
[48] T.P. Sullivan, W.H. Eaglstein, S.C. Davis, P. Mertz, The pig as a model for human wound healing, Wound Repair Regen. 9 (2) (2001) 66–76, https://doi.org/10.1046/j.1524-475x.2001.00066.x.
[49] W. Ren, V. Messerschmidt, M. Tsipursky, J. Irudayaraj, Oxygen nanobubbles-embedded hydrogel as wound dressing to accelerate healing, ACS Appl. Nano Mater. 6 (14) (2023) 13116–13126, https://doi.org/10.1021/acsanm.3c01812.
[50] P. Kong, X. Xie, F. Li, Y. Liu, Y. Lu, Placenta mesenchymal stem cell accelerates wound healing by enhancing angiogenesis in diabetic Goto-Kakizaki (GK) rats, Biochem. Biophys. Res. Commun. 438 (2) (2013) 410–419, https://doi.org/10.1016/j.bbrc.2013.07.088.